



Open Archive TOULOUSE Archive Ouverte (OATAO)

OATAO is an open access repository that collects the work of Toulouse researchers and makes it freely available over the web where possible.

This is an author-deposited version published in : <http://oatao.univ-toulouse.fr/>
Eprints ID : 4746

To link to this article : DOI :10.1016/j.corsci.2010.08.013

URL : <http://dx.doi.org/10.1016/j.corsci.2010.08.013>

To cite this version : Fedorova, E. and Monceau, Daniel and Oquab, Djar (2010) *Quantification of growth kinetics and adherence of oxide scales formed on Ni-based superalloys at high temperature*. Corrosion Science, vol. 52 (n° 12). pp. 3932-3942. ISSN 0010-938X

Any correspondance concerning this service should be sent to the repository administrator: staff-oatao@inp-toulouse.fr.

Quantification of growth kinetics and adherence of oxide scales formed on Ni-based superalloys at high temperature

E. Fedorova^{a,b}, D. Monceau^{b,*}, D. Oquab^b

^a Polytechnic Institute of Siberian Federal University, 660074 Krasnoyarsk, Russia

^b Institut Carnot CIRIMAT, ENSIACET, 31030 Toulouse Cedex 4, France

A B S T R A C T

Cyclic and isothermal oxidation behaviors of first and fourth-generation superalloys AM1 and MCNG were investigated to evaluate the ability of the scratch test to quantify the adhesion of multi-layered oxide scales. Effects of sulfur content and of scale thickness were studied independently. Available models lead to large discrepancies in the calculated work of adhesion values with the evaluation of the residual stress being the largest source of error. Nevertheless, models can assess the effect of sulfur content and the scratch test can be used to correlate the long-term cyclic oxidation behavior and the adhesion of oxide scales.

Keywords:

A. Nickel
A. Superalloys
C. Oxidation
C. Interfaces
B. SEM

1. Introduction

Oxidation resistance of Ni-based superalloys and bond coating materials in high-temperature environments is largely dictated by their ability to preferentially form an adherent oxide scale on the metal surface [1]. Maintaining good adhesion of the oxide scale to the surface of heat-resistant alloys is crucial for long-term cyclic oxidation resistance. Single crystal Ni-based superalloys have been developed firstly for their mechanical properties. For application as blade materials, single crystals are usually coated to improve their hot corrosion and oxidation resistance. However, cracking of the coating or removal by abrasion or by foreign object damage (FOD) can occur so that the intrinsic oxidation behavior of bare single-crystal superalloys must be accurately known [2].

The oxide scale adhesion depends on the alloy sulfur content and its presence at the oxide/alloy interface [3,4]. Indeed, it was shown that sulfur removal improves scale adhesion if its concentration is below 0.1–1 ppm in weight, depending on the thickness of the samples [5,6]. It is also well known that the detrimental effect of S can be overcome by appropriate additions of reactive elements, such as Zr, Y, or Hf to the alloy [5–7].

Scratch test as an appropriate method for qualitative evaluation of the film adhesion to substrate has been used in many studies [8–16]. Both intrinsic parameters, such as scratching speed, loading rate, diamond tip radius, and extrinsic parameters, such as substrate hardness, coating thickness, substrate and coating roughness

and coefficient of friction, were considered, in the literature, to improve the interpretation of the results.

The main objective of the present study is to evaluate the ability of the scratch test to quantify the adherence of oxide scale formed on Ni-based superalloys. The long term objective of this work is to establish the relationship between oxide scale/alloy adhesion, isothermal oxidation kinetics of the alloy, physical properties of the alloy and the oxide, and cyclic oxidation performance of the superalloys.

2. Experimental procedure

2.1. Materials

Single crystal Ni-based superalloys AM1 with different sulfur concentrations and MCNG containing 0.1 wt.% Hf were provided by Snecma-Safran Group. The sulfur content for AM1 alloy ranges from 0.22 up to 3.2 ppmw as measured by glow-discharge mass spectroscopy (GDMS). AM1 is a first-generation Ni-based single-crystal superalloy whereas MCNG refers to a fourth-generation single-crystal superalloy containing Ru and Re and some Hf. The chemical compositions of the superalloys are presented in Table 1. Disk-shape samples of 11–13 mm diameter and 1 mm thick were machined along the [0 0 1] direction from rods.

Prior to oxidation, all sides of the specimens were ground with SiC paper down to a final grade 600 or ground and then polished down to a 1 μ m finish using diamond paste. All samples were cleaned in an ultrasonic bath with acetone followed by high-purity alcohol. They were weighed to within 10 μ g with a Sartorius ME balance before and after high-temperature exposures.

* Corresponding author. Tel./fax: +33 5 34 32 34 22.

E-mail address: daniel.monceau@ensiacet.fr (D. Monceau).

Table 1

Chemical composition of the single crystal Ni-based superalloys AM1 and MCNG (wt.%).

Alloys	S (ppmw)	Cr	Co	Mo	W	Ta	Al	Ti	Re	Ru	Hf	Ni
AM1	0.22 0.41 3.20	7.5	6.5	2	5.5	8	5.3	1.2	–	–	–	Base
MCNG	0.53	4	–	1	5	5	6	0.5	4	4	0.1	Base

2.2. Thermogravimetry and cyclic oxidation tests

The isothermal thermogravimetric tests were performed in a SETARAM™ TAG 24S thermobalance with a sensitivity of greater than 1 µg. The device makes use of a double symmetrical furnace designed to compensate all signal disturbances resulting from gas flow, buoyancy and convection. It is suitable for the accurate measurement of small mass changes occurring during short oxidation tests or induced by very slow-growing oxide scale such as the alumina scale formed on superalloys. The samples were oxidized at 1100 °C under a flow of synthetic air with a heating rate of 60 °C min⁻¹. The flow rate was maintained at 0.4 l/h.

The AM1 specimens with three different sulfur levels and the 1 µm polished surface finish were oxidized for 9, 17 and 18 h to form oxide scales of similar thickness. The continuous recording of the mass gain within the thermobalance allowed stopping the experiments when the desired oxide scale thickness was reached. This was done to investigate the effect of sulfur content on adhesion independently of oxide thickness (Table 2). To examine the changes of adhesion values as a function of scale thickness, specimens of alloys AM1 (0.41 ppm S) and MCNG were oxidized for different exposure times. The effect of surface finish was also studied on samples of AM1 (0.41 ppm S) and MCNG with similar isothermal oxidation durations of 90 and 100 h (Table 2).

Cyclic oxidation tests were conducted in a previous study on specimens coming from the same alloy batch [17]. A thermal cycle consisted of a fast heating period at 90 °C/min up to 1100 °C (transfer of the samples to the hot zone in 10 s), a 60 min exposure at 1100 °C (including heating) in laboratory air, followed by a 15 min fast (800 °C/min) cooling to room temperature in a strong flow of purified air.

2.3. Microstructure and morphology characterization

The use of a thermogravimetric device allows to detect if the samples experience spalling during the high temperature dwell and even during cooling. In the present case, no such spalling event

was detected, it was then possible to determine the total oxide scale thickness t from the difference of the mass at the beginning of oxidation and at the end of the process inside the thermobalance. The value of t was then verified from the direct observation using scanning electron microscopy (SEM) on a LEO 435VP system in conventional mode. The microstructure of the oxide scales formed on AM1 and MCNG were characterized. When the oxide scale was duplex, i.e. consisting of an inner alumina layer in contact with the metal and an outer spinel layer, the thickness of the internal pure Al₂O₃ ($t_{\text{Al}_2\text{O}_3}$) layer was measured by SEM (Table 2). The oxide phases were identified by X-ray diffraction (XRD) using a Seifert 3000TT diffractometer operated at 40 kV and 30 mA at a low angle of incidence (4°) in order to maximize the relative intensities of the oxide scale peaks and to ensure that the analyzed depth did not depend on Bragg's angle. The chemical analysis by means of a PGT (imix-PC) system for the EDS was performed as a complementary study.

2.4. Scratch test

To evaluate the mechanical adherence of the oxide scale formed on AM1 and MCNG alloys, the scratch test was carried out using a commercial SCM Revetest scratch tester. A Rockwell diamond indenter with a 200 µm radius hemispherical tip was used. The normal load F_n was continuously increased from 1 N up to 100 N. The loading rate was 50 N/min. A 3 mm long scratch was made during each test. The instrument is equipped with an integrated optical microscope, an acoustic emission monitoring system to detect crack formation and a device to measure the horizontal frictional force F_t in the scratching direction from which the friction coefficient values μ can be obtained ($F_t = \mu F_n$). The critical load criterion used was the lowest load at which failure occurred along the scratch track as determined by optical microscope examination. The first acoustic emission peak observed and the variation of the frictional force provide complementary information for critical load measurements. Five scratches were performed for each sample under the test conditions determined previously. Average

Table 2

Conditions of the isothermal oxidation experiments and obtained oxide scale thicknesses (see text).

Alloy	Sample No.	Sulfur content, ppmw	Surface finish	Isothermal oxidation at 1100 °C, h	Total scale thickness ^a , t , µm	Thickness of internal α -Al ₂ O ₃ layer $t_{\text{Al}_2\text{O}_3}$, µm
AM1	1	0.22	1 µm	18	1.1	~0.7
	2		600 SiC	100	1.6	n.m. ^b
	3	0.41	1 µm	9	1.3	~0.7
	4			100	2.4	~1.4
	5			330	3.6	~1.7
	6		600 SiC	100	2.7	n.m.
	7	3.2	1 µm	17	1.3	~0.8
	8		600 SiC	100	1.6	n.m.
MCNG	1	0.53	1 µm	0	1.1	0
	2			3	1.7	0
	3			10	1.9	~0.2
	4			100	2.6	~0.6
	5		600 SiC	90	2.1	n.m.

^a Calculated from TGA data.^b Not measured.

values of critical normal load, corresponding frictional force, coefficient of friction, and track width are reported. A schematic representation of test and data recording during the experiment is shown in Figs. 1. Point “A” corresponds to the smallest load at which some recognizable adhesive failure event occurs. Point “B” corresponds to a load of 40 N and point “C” to the end of scratch.

3. Results and discussion

3.1. Oxidation behavior

To investigate the cyclic oxidation behavior, it is necessary to know both the isothermal oxidation kinetics of the studied alloys and the adherence of oxide scales formed on their surfaces.

Results for cyclic oxidation kinetics of AM1 and MCNG samples are compared in Fig. 2. The cyclic oxidation behavior of the AM1 alloy showed the expected improvement in scale retention as the sulfur concentration was decreased. After 430 cycles, the samples with 3.2 ppmw S presented significant oxide spallation with an average weight loss of 17 mg/cm² (not shown in Fig. 2) whereas the sample with 0.22 ppmw S, weight loss was 0.03 mg/cm². For the MCNG sample, a low mass change and good scale adherence

was observed despite the fact that it contains 0.53 ppmw S. This is certainly due to beneficial effect of Hf [5–7] and/or to the presence of Rh and Ru.

The net mass gain curves obtained during isothermal oxidation at 1100 °C for AM1 and MCNG alloys (Fig. 3) showed faster oxidation kinetics over the transient regime for all the samples. After ~6 h, oxidation kinetics of both alloys follows a parabolic law. Then, the parabolic constants k_p were calculated by fitting a complete parabolic law after the transient regime, using:

$$t = A + B(\Delta m/S) + (1/k_p)(\Delta m/S)^2 \quad (1)$$

where t is the time, A and B are constants and $(\Delta m/S)$ is the mass variation of the sample divided by its surface area [18]. The steady-state parabolic rate constants (k_p) calculated from thermogravimetric analysis data for AM1 with different levels of sulfur and for AM1 and MCNG with different surface finishes are compared in Table 3. As seen in Fig. 3b and Table 3, the oxidation kinetics of AM1 specimens are not monotonous functions of the sulfur level. Indeed, the highest oxidation kinetics are found for the AM1 sample with the intermediate sulfur level. This result can be explained in terms of materials processing differences resulting in different impurity levels for this series of rods, but no precise data are

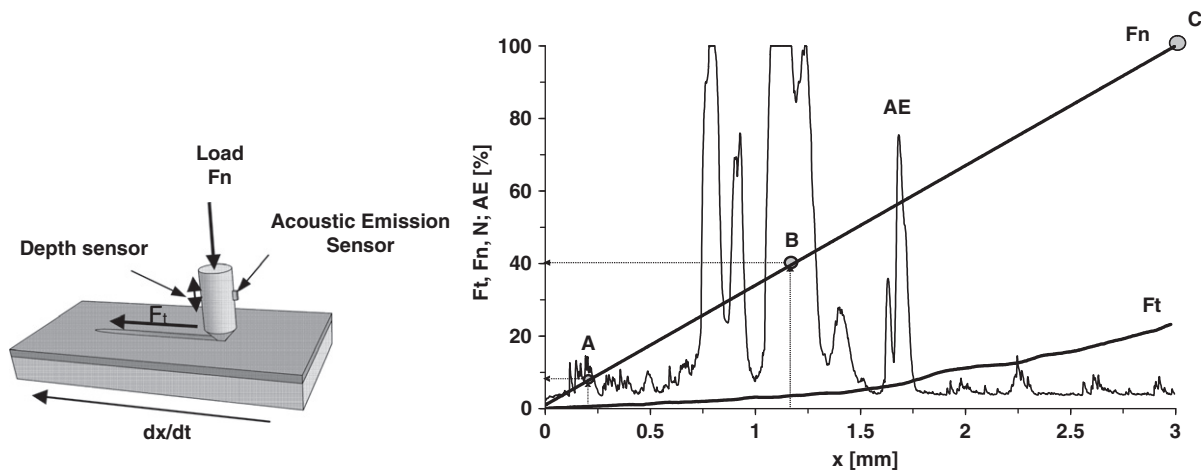


Fig. 1. Schematic presentation of the scratch test and an example of data recorded during the scratch test: F_t – frictional force; F_n – normal load; AE – signal of acoustic emission; x – scratch length. Point A – critical load; B – 40 N load; C – end of scratch.

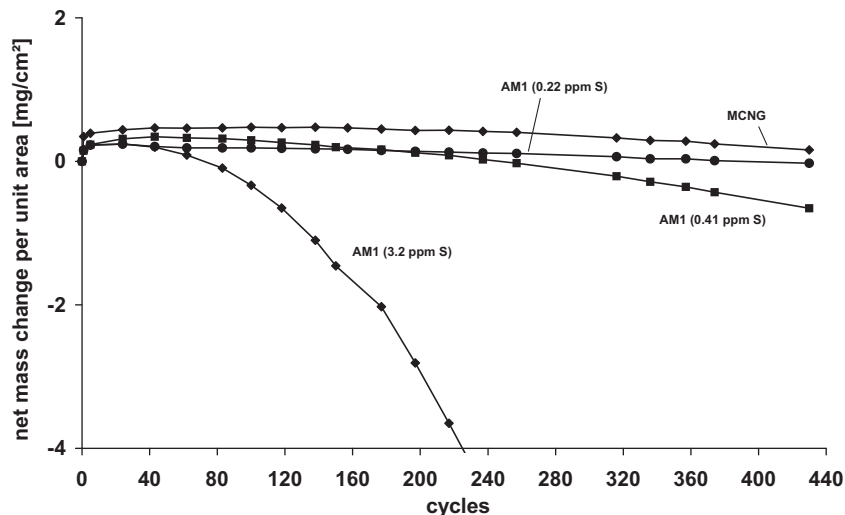


Fig. 2. Cyclic oxidation kinetics of superalloys AM1 and MCNG (1 h cycles at 1100 °C) [17].

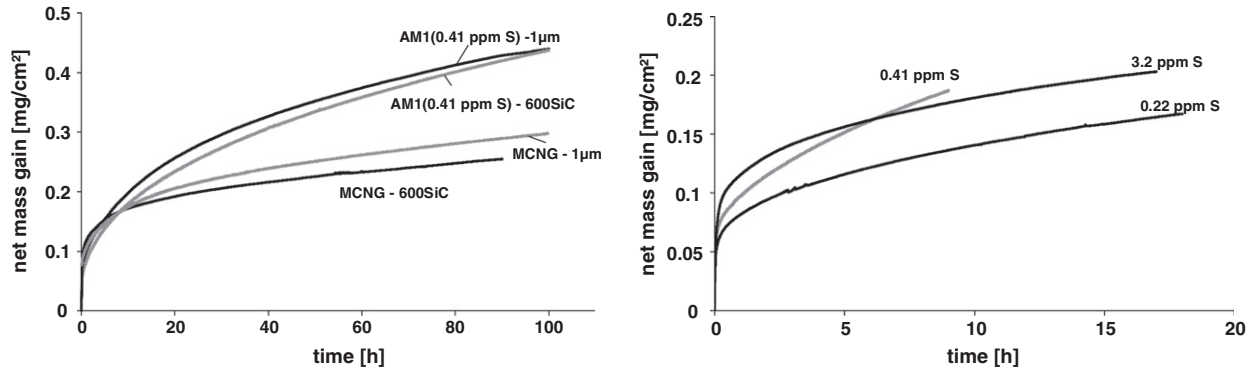


Fig. 3. Isothermal oxidation kinetics at 1100 °C in synthetic air flow (a) AM1 and MCNG superalloys with different surface finish (label: superalloy (wt ppm of S) – polishing), (b) AM1 with different sulfur content. Mass gain during heating is not included.

Table 3

Stationary values of parabolic rate constants k_p , at 1100 °C, calculated between 6 h and the end of the experiment using $t(s) = A + B (\Delta m/S) + (1/k_p) (\Delta m/S)^2$.

Alloys, sample No.	Sulfur content, ppmw	Surface finish	Isothermal oxidation exposure at 1100 °C, h	k_p , mg ² /cm ⁴ /s	B , s cm ² /mg	A , ks
AM1	0.22	1 μm	18	1.4×10^{-7}	-12.1×10^5	60
		600 SiC	100	1.1×10^{-7}	-18.1×10^5	110
	0.41	1 μm	100	2.6×10^{-7}	-11.5×10^5	110
		600 SiC	100	3.3×10^{-7}	-6.3×10^5	50
	3.2	1 μm	330	1.8×10^{-7}	-18.5×10^5	200
		1 μm	17	1.1×10^{-7}	-23.9×10^5	170
		600 SiC	100	0.8×10^{-7}	-33.3×10^5	250
		600 SiC	100	0.6×10^{-7}	-48.2×10^5	400
MCNG	0.53	1 μm	100	0.6×10^{-7}	-48.2×10^5	400
		600 SiC	90	0.4×10^{-7}	-81×10^5	620

available. In agreement with the data presented, the k_p values for the Hf-containing MCNG alloy were lower than the values measured for all AM1 samples despite the fact that the initial oxidation rate of MCNG was higher than that of AM1. Similar effect was also reported by Hayashi and Gleeson for Hf-containing Pt-modified γ/γ' alloys [19] for which a high oxidation rate during the transition stage was found. No effect of surface finish (600 grit SiC or 1 μm diamond) on the oxidation kinetics was detected (Fig. 3a).

3.2. Microstructures of oxide scales

During oxidation of nickel-based superalloys, a multi-layered oxide scale forms [2,20,21]. Back-scattered and secondary electron images of the oxide scales formed on the surface of AM1 and MCNG alloys after 100 h isothermal oxidation at 1100 °C are presented in Fig. 4. EDS analysis and X-ray diffraction were used to identify phases. In the case of AM1 alloy, the oxide consists of an inner alumina layer in contact with the metal and an outer NiAl₂O₄ spinel layer separated by discontinuous (Ta, Ti)-rich oxide (bright spots on BSE images Fig. 4a). TiO₂ was also identified by XRD so the (Ta-Ti)-rich oxide is certainly a rutile phase. On MCNG alloy, the oxide scale was composed of three clearly distinct layers (Fig. 4b). The inner adherent layer is α -Al₂O₃, which its morphology is shown in a higher magnification in 5. The outer layer of the scale is NiO. Between them is located a double layered NiAl₂O₄ spinel separated by a discontinuous (Ta, Ti)-rich oxide, with some Re- and Ru-rich particles, which were also identified by EDS. The XRD analysis of this oxidized MCNG sample showed the presence of α -Al₂O₃, TiO₂/TiTaO₄ rutile, NiAl₂O₄ spinel, and NiO in the scale.

3.3. Assessment of the work of adhesion of oxide scales using the scratch technique

The interpretation of scratch-test results can be misleading. In order to correctly choose the test parameters and to assess the

work of adhesion using the scratch technique understanding the limits of validity of the results, it is mandatory to review the existing models and their physical assumptions. Theoretical models based on the Linear Elastic Fracture Mechanics approach and different adhesion testing techniques including the scratch test for variety of systems were reviewed by Volinsky et al. [22]. The scratch test has been used to measure the adherence of a range of coatings on steel substrates, such as, hard coatings TiN [23–28], CrN and CrN/Cr [23,26,29], TiC or/and TiC/CrC [10,23], thermally grown Al₂O₃ [24], diamond-like carbon (DLC) on WC-Co substrate [30] and more recently polymeric coating [31]. In common practice, the scratch test is used for comparative studies of thin films of the same thickness on identical substrates. The mechanical behavior of thin film/substrate systems under sliding indenter loading is complex. Difficulties include complicated stress-strain field, different failure modes occurring at the same time, numerous intrinsic and extrinsic parameters. Therefore, the technique is usually regarded as semi-quantitative. The earliest model developed by Benjamin and Weaver [8] uses the theory of fully plastic indentation and gives an expression for the critical shearing force for coating removal [32]. This model is applicable in a limited range of cases for plastically deformed film. The model was developed further by Weaver to include the elastic properties of the coating and assuming elastic-plastic behavior in the system during scratching. The best parameter for the quantitative evaluation of the adhesion strength between a film (coating or oxide scale) and a substrate is the work of adhesion, which is a measure of the chemical bonding across the interface [33].

In the present study, the most commonly used models to assess the work of adhesion during scratch test were analyzed. A brief description of these models is presented below. The great number of theoretical models employed to calculate the work of adhesion are based on the Griffith energy balance approach [34,35] developed by Orován [36] and Irwin [37], which relates the elastic strain energy released to the surface energy for crack formation.

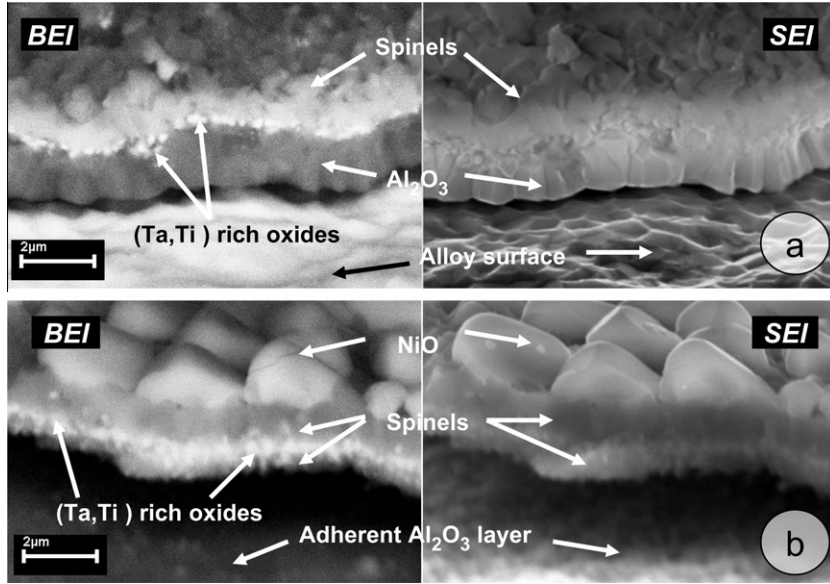


Fig. 4. SEM micrographs of the oxide scales formed on AM1 (a) and MCNG (b) after 100 h isothermal oxidation at 1100 °C in synthetic air (see text for the details).

Application of this approach to estimate the coating/substrate adhesion in the scratch test was proposed by Laugier [10]. The load, at which failure occurs, termed the “critical load”, is used to assess the work of adhesion. During the test, at critical load, the film ahead of the indenter releases its elastic deformation energy by interface delamination and film spallation. The stylus adds compressive stress to the film in front of the indenter. It is important to note that in most cases, the film or oxide scale already has some residual compressive stresses with some consequences detailed below. The critical load depends not only on the adhesion property of a considered film/substrate pair but also on several parameters related to the testing conditions – as indicated above – and to the elastic–plastic behavior of each material. Thus, it produces a measurement of the practical work of adhesion. The elastic energy per unit volume (U) stored in a film is expressed as:

$$U = \frac{\sigma^2}{2E_f} \quad (2)$$

where σ is the stress responsible for interface failure and E_f is Young’s modulus of the film.

The elastic energy stored in the entire film of thickness t is given as:

$$U = \frac{\pi r^2 t}{2} \left(\frac{\sigma^2}{2E_f} \right) \quad (3)$$

where r is the radius of the semicircle, which is formed in front of the indenter under the critical load, and is equal to one-half of the scratching width. This equation is theoretically valid for the substrate region occurring either in the elastic or the plastic deformation. When the normal load applied in the indentation test reaches the critical load, the elastically stored energy U in the entire film is equal to the total energy of adhesion (W_{fs}). Theoretically, the adhesion energy (W_{fs}) represents the elastically stored energy arising in the elastic and plastic substrate regions of deformation.

The differences between the models described in the present work are based on the method employed for the evaluation of the local stress. In the purely elastic analysis of Laugier [10], the compressive stress in the film is a function of the internal stress and the applied stresses which were calculated from the equation of Hamilton and Goodman [38]. Contact radius was taken from the

contact theory of Herth [39], which is formulated on the assumption of elastic deformation between two bodies in contact. This model was criticized by Rickerby [25] in view of limitations in application to materials that deform plastically. Later, the model of Laugier was modified by Gruss and Davis [40] who introduced the equation for the indentation stress of elastic–plastic homogeneous materials developed by Chiang et al. [41] and employed it to calculate the work of adhesion of polycrystalline ZrN and amorphous SiC coatings on nickel and titanium alloys, i.e. a hard ceramic layer on a more ductile metallic substrate as for an oxidized metal. It was observed [40] that the modified model, in comparison with Laugier’s model, produces similar values of adhesion work.

It is well known that a range of possible failure modes can occur during the scratch test and only some of these are dependent on scale–substrate adhesion. According to Burnett, Rickerby, and Bull [14,24], the adhesion related compressive failures which are the basis for hard coatings on a softer substrate are buckling and spallation by wedging. The theoretical basis to analyze buckle failure was developed for oxide scales under thermally induced stresses [42–44] from the classical buckling analysis of Timoshenko in 1936 [45]. Wedge spallation failure mode (compressive shear crack and spall after shear cracking) and local stress analysis was carried out by Evans [44]. In order to quantify adhesion measurement, a careful analysis of the observed failure modes is needed. However, the validity of direct application of this approach, which was developed for the thermal and growth biaxial stresses for scratch induced stresses assessment, can be questioned. Moreover, this method requires precise measurements of the area and geometry of delamination which is not always easy to determine when the different failure modes occur at the same time.

Scratch testing can be regarded in relation to the delamination of films under static indentation. A number of models have been developed to relate the interfacial toughness to the critical indentation load required for debonding [46,47]. These models rely on the fact that the indentation volume is accommodated by plastic deformation around the indenter within the plane of film. This deformation establishes residual elastic stress which can provide a driving force for delamination and spalling [32]. Some of these concepts have been extended to the scratch. Burnett and Rickerby developed the analysis based on the elastic–plastic indentation theory [14,15] and identified three components for the total stress

responsible for coating detachment during the scratch test. First, a static elastic-plastic indentation stress, second, a tangential frictional stress due to the interaction between the sliding indenter and the specimen surface and third, the residual internal stresses in the film. This analysis was extended by Bull et al. [48] and later refined by Bull and Rickerby [49]. Each one of the three contributions described before was expressed in terms of its effect on the measured total frictional force F_t . Indentation stress, often named “ploughing stress”, has been considered as the component of stress responsible for film delamination. Accordingly, the local compressive stresses in the plane of the interface or the tensile stresses normal to the interface, due to Poisson’s effect, cause the oxide/scale detachment:

$$\sigma = \frac{\nu_f F_t}{A_1} \quad (4)$$

where ν_f is the Poisson ratio of the film; A_1 is the cross-sectional area of the track, which can be calculated using the indenter radius R and the track width d_c measured at critical load F_{nc} :

$$A_1 = R^2 \sin^{-1} \left(\frac{d_c}{2R} \right) - \frac{d_c}{2} \left[R^2 - \left(\frac{d_c}{2} \right)^2 \right]^{1/2} \quad (5)$$

The final equation which relates the minimum critical load with the practical work of adhesion, W , is:

$$F_{nc} = \frac{A_1}{\nu_f \mu_c} \left[\frac{2E_f W}{t} \right]^{1/2} \quad (6)$$

where $\mu_c = F_t/F_{nc}$ is the friction coefficient corresponding to the critical load.

This model has been modified by Attar and Johannesson [23] using an equation which, in contrast to Eq. (6), shows a direct proportionality between the critical normal load and the square root of the coating thickness:

$$F_{nc} = \frac{d_c}{\nu_f \mu_c} [2E_f W t]^{1/2} \quad (7)$$

A combination of shear and tensile stresses in the coating/substrate interface ahead of the indenter and the possibility of plastic deformation occurring in the coating were assumed. In this model, the frictional force acts on the cross-section of the coating $A = t d_c$ [23].

Before to apply these models to the oxidized superalloys, it is then necessary to observe the failure modes which have occurred during the scratch tests.

3.4. Qualitative results of scratch tests

For the studied oxide scale/substrate systems, two adhesion-related failure modes occurring in the test were observed during the scratch track examination. First, the interfacial spallation at the border of the scratch track and second, the conformal type buckling cracks. In many cases, it is difficult to identify the predominant failure mode. Nevertheless, the complex morphology of the cracks observed can be considered as a response by buckling as the main failure mechanism induced by compressive stresses ahead of the moving indenter. Large area interfacial spallation was observed for the oxide scale formed on AM1 with 0.41 and 3.2 ppmw S (Fig. 6).

The load at which failure occurs is firstly used for a qualitative analysis. As already established [11,12,33], the critical load is factored by intrinsic parameters, including loading rate and scratch velocity. In the present study the operating parameters of the scratch test were determined previously and were fixed. Thus the critical load depends on the combined effect of the oxide scale thickness and the oxide/scale adhesion. Values measured during the scratch test for AM1 and MCNG are presented in Tables 4 and 5 respectively.

Table 4

Average values^a of critical load measured during the scratch test and calculated values of the work of adhesion for AM1 samples polished down to 1 μm finish and oxidized in different conditions.

AM1 sample No.	Sulfur content, ppmw	Oxide scale thickness t , μm	Critical load F_{nc} , N	Work of adhesion W , J m^{-2}	
				Model 1	Model 2
<i>Effect of sulfur content, $t = \text{const}$</i>					
1	0.22	1.1	19.5 ± 1.1	2.2	21.7
3	0.41	1.3	14.6 ± 1.2	2.0	11.4
7	3.2	1.3	10.0 ± 0.5	1.8	6.5
<i>Effect of scale thickness, $S_{\text{content}} = \text{const}$</i>					
3	0.41	1.3	14.6 ± 1.2	2.0	11.4
4		2.4	11.6 ± 0.6	2.8	3.5
5		3.6	9.8 ± 1.3	3.9	1.8

^a Five scratches were performed for each sample.

Table 5

Average values^a of critical load measured during the scratch test and calculated values of the work of adhesion for MCNG samples polished down to 1 μm finish and oxidized in different conditions. Critical load is given for the external spinel layer (t_{ext} – thickness of external spinel layer) and for the internal alumina layer (when present).

MCNG sample No.	Oxide scale thickness, μm	Critical load F_{nc} , N	Work of adhesion W , J m^{-2}			
			Model 1	Model 2		
1	t_{ext}	1.1	F_{nc1}	5.4 ± 0.4	0.5	1.4
	$t_{\text{Al}_2\text{O}_3}$	0	F_{nc2}	–	–	–
2	t_{ext}	1.7	F_{nc1}	9.7 ± 0.6	1.0	2.0
	$t_{\text{Al}_2\text{O}_3}$	0	F_{nc2}	–	–	–
3	t_{ext}	1.7	F_{nc1}	20.3 ± 0.4	2.8	11.3
	$t_{\text{Al}_2\text{O}_3}$	~ 0.2	F_{nc2}	65.0 ± 2.1	0.1	306
4	t_{ext}	2.6	F_{nc1}	8.9 ± 0.4	3.2	2.2
	$t_{\text{Al}_2\text{O}_3}$	~ 0.6	F_{nc2}	29.4 ± 1.6	0.5	33

^a Five scratches were performed for each sample.

The variation of surface roughness due to different surface finishes has the same effect on the values obtained for the critical load for both AM1 and MCNG samples. A rough surface (600 grit SiC grinding) decreases the reading and repeatability of measured values, showing lower value of critical load compared with samples polished down to 1 μm finish.

For the oxide scales with a constant thickness and a surface finish of 1 μm , different critical normal and tangential forces were measured depending on the sulfur level. There was a clear tendency for the critical load to decrease with increasing sulfur content. Optical observations of detachment development show large areas of spallation at early load for the oxide scale grown on the AM1 alloy with the highest sulfur level. At the end of the test, the oxide scale was completely removed from the substrate. AM1 containing 0.22 ppmw S was considerably more resistant to detachment in comparison with 3.2 ppmw S sample (Fig. 6). These qualitative results are in good accordance with the cyclic oxidation kinetics reported in Fig. 2 and numerous data reported in the literature ([3,4,20]). The role of sulfur is likely associated with a reduction in fracture toughness of the oxide/metal interfaces through formation of voids or reduction of the bonding energy [20].

The effect of coating thickness is usually discussed in publications related to the scratch test application or modeling. Detailed analysis of thickness dependence has been studied by several authors [14,15]. For coatings of variable thickness, the energy balance approach predicts that F_{nc} decreases, since internal energy increases with increasing thickness according to [25,30,50]. Nevertheless, the critical load for hard, wear-resistant coatings is generally found to increase with increasing coating thickness, e.g. [23]. The influence of thickness on the failure mode was observed by [24]. It was found that the critical load for buckle formation increases as the thickness increases and decreases for wedging failure. A more complex relationship between these two parameters affected by conditions of film deposition was observed [51].

In the case of oxidized AM1 samples, Table 4 shows that increasing scale thickness, for a constant sulfur level and identical

surface finish, causes the decrease of the critical load. This observation was confirmed by optical and SEM characterizations showing that the oxide scale spalled area enlarges with the duration of isothermal oxidation.

It is important to point out that the studied case of oxide scale adherence on an alloy is more complex than that of a film deposited on a substrate. For a thermally grown oxide, it may be necessary to distinguish the effect of oxide scale thickness and the effect of oxidation duration on the adhesion behavior. Indeed, the metal/oxide interfacial adhesion may evolve during oxidation with alloying element depletion and subsequent phase transformation [52], with cavity formation [53], sulfur segregation [54], substrate plastic deformation [55] and/or oxide scale wrinkling which was observed in the case of oxidation of uncoated single-crystal superalloy [52]. Moreover, growth and thermal residual stresses [44] should be considered. In our case, the tilted surfaces of oxidized superalloys after spalling were observed and no wrinkling or cavity formation was observed. Sulfur segregation was not measured. The most obvious observation was the multi-layered nature of the oxide scale.

The multilayered structure of the oxide scale must be accurately known for a correct analysis of scratch-test results. Indeed, the layering of the oxide scale influences the values measured for the critical load. It is important to notice that the different sublayers of the oxide scale remained adherent to each other for the AM1 samples whereas the fracture occurred between the internal alumina layer and the outer spinel layer for the MCNG ones (Fig. 4 and 5). Representative fracture cross-sections of the oxide scale after the scratch test from MCNG (SE and BSE images) show the entire oxide scale structure in contact with the metal and magnified images of the inner adherent alumina layer (Fig. 5). Despite the spalling of the external spinel oxide layer, MCNG alloy containing 0.53 ppmw S and 0.1 wt.% Hf demonstrates noticeably better performance than AM1 with about the same concentration of sulfur (0.41 ppmw) under the same conditions of oxidation. This is clearly due to the better adherence of the internal alumina subscale. When applying the

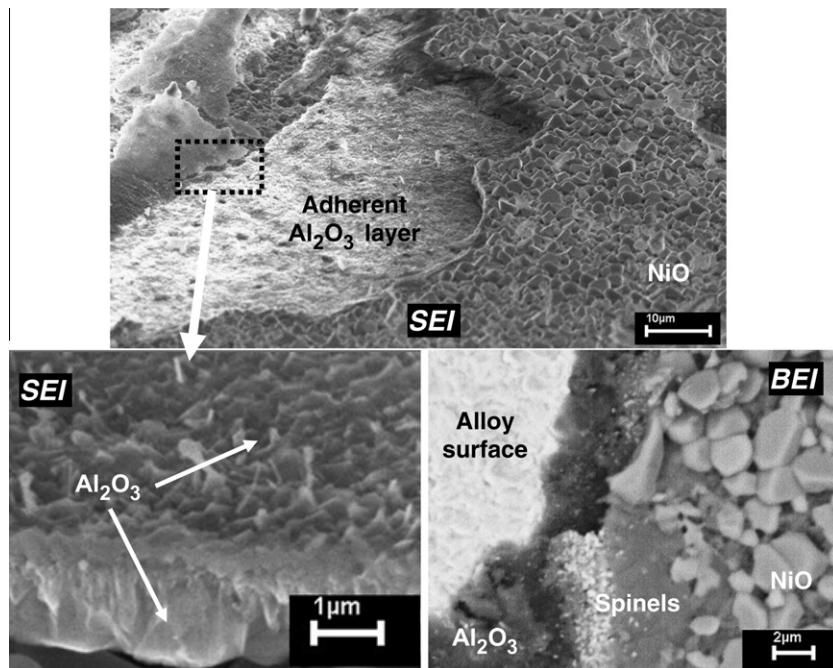


Fig. 5. Micrographs showing the oxide scale spallation on the MCNG isothermally oxidized for 100 h at 1100 °C, after scratch test (upper image); the lower left image shows the fractured continuous internal alumina layer; the lower right image indicates an area where the whole oxide scale is broken. The dark grey layer is the internal alumina layer, the intermediate grey is the double layer of spinels and the bright grains are nickel oxide. The very bright small sized particles inside or over the spinel layer are (Ta-Ti) rich oxides.

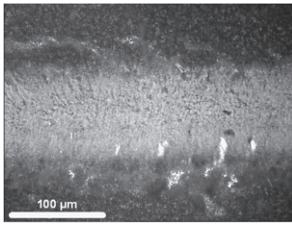
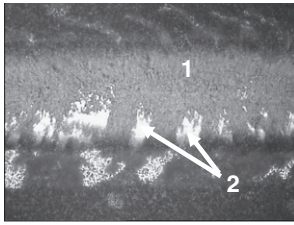
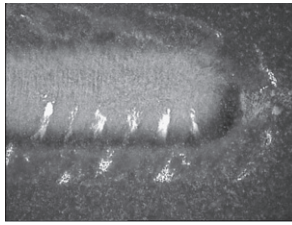
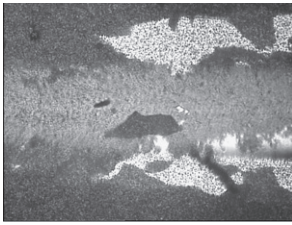
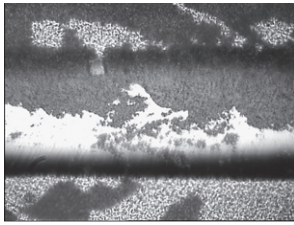
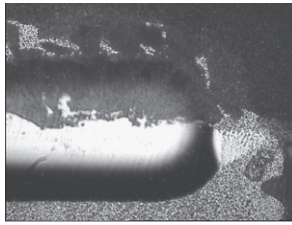
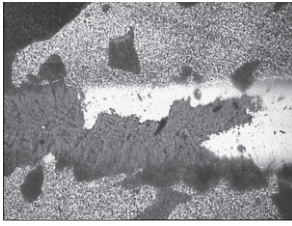
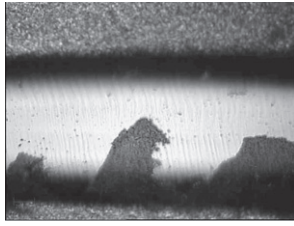
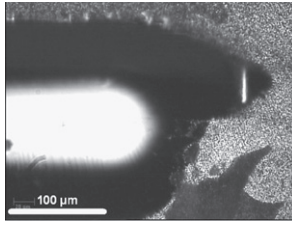
AM1, ppmw S and critical load	A Beginning of spalling	B Spalling evolution $F_n = 40$ N	C End of the scratch
0.22 $F_{nc} = 20$ N			
0.41 $F_{nc} = 15$ N			
3.2 $F_{nc} = 10$ N			

Fig. 6. Optical micrographs showing the oxide scale spalling induced by the scratch test for AM1 samples with different sulfur contents: 1 – oxide scale; 2 – alloy surface.

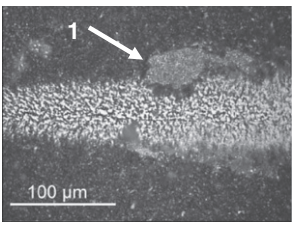
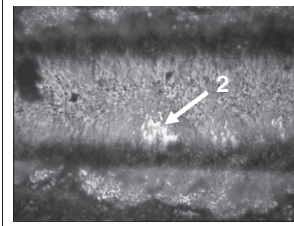
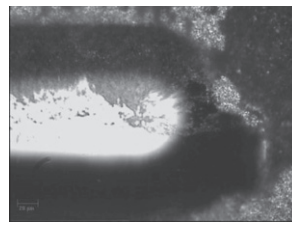
MCNG critical load	A Beginning of spalling	B Spalling evolution $F_n = 40$ N	C End of the scratch
$F_{nc1} = 9$ N $F_{nc2} = 30$ N			

Fig. 7. Optical micrographs showing the oxide scale spalling induced by the scratch test for MCNG samples oxidized 100 h at 1100 °C: 1 – external spinel layer spalled at $F_{nc1} = 9$ N; 2 – internal alumina layer spalled at $F_{nc2} = 30$ N.

scratch test to MCNG samples, the two oxide sublayers spalled at different loads, as reported in Table 5. The external spinel layer spalled at a critical load equal to or smaller than the load for the oxide scale on AM1. For example, the critical normal load for the MCNG sample was 9 N but was 12 N for the AM1 sample oxidized in the same conditions (100 h at 1100 °C). But, the internal alumina layer formed on MCNG spalled at a much higher critical load (30 N) (Fig. 7). Therefore, Table 5 gives two lines of values measured for each MCNG sample. The first corresponds to the total scale and the second to the internal alumina layer thickness. The fact that spalling can occur at the subscale interfaces is of great importance for the quantitative analysis.

In general, the critical loads for MCNG were decreased when a characteristic oxide scale thickness, at which a large spallation

occurred, was exceeded. This tended to occur when the oxide scale failure was dominated by the stress levels already present within the scale.

3.5. Quantitative results of scratch tests

Here, we apply the models discussed in a previous section, to quantify the adherence of oxide scales formed on AM1 and MCNG superalloys. To understand the problems that arise during the interpretation of scratch-test results, the most commonly used models were chosen as the basis for the present adhesion analysis. The work of adhesion was estimated using the models described in Eqs. (6) and (7) (Models 1 and 2 correspondingly), and assuming the following elastic properties: Young's modulus of bulk alumina

$E_f = 380$ GPa, and Poisson ratio $\nu_f = 0.24$ were used for the oxide scale [56]. The mechanical properties of scale formed on the alloy surface were not measured in the present work. This would be a source of improvement for further analysis.

3.5.1. Effect of sulfur content at constant oxide scale thickness

The results obtained for AM1 samples are presented in Table 4. Both models (Eqs. (6) and (7)) show a tendency towards a decreasing work of adhesion with increasing sulfur content. As seen in the qualitative analysis, this is in agreement with the cyclic oxidation kinetics as well as with the optical and SEM observations after the scratch test on isothermally oxidized samples. According to Table 4, the values of the work of adhesion calculated with the model of Bull and Rickerby (Eq. (6)) are very small in comparison with those given in Attar and Johannesson's model (Eq. (7)). For example, for specimen 1 of the AM1 series (AM1-1), the value of W given by Eq. (6) was 2.2 J/m^2 and by Eq. (7) was 21.7 J/m^2 . For the values presented in Table 4, scale residual stresses σ_R , were not considered. If it is assumed that the oxide scale has the same elastic and dilatation properties as $\alpha\text{-Al}_2\text{O}_3$, the value of the TGO residual stresses can be estimated from the thermal expansion mismatch between the thin oxide layer and the thick substrate [57]. The thermal stresses in first approximation:

$$\sigma_f = \frac{E_f \Delta T \Delta \alpha}{1 - \nu_f} \quad (8)$$

where ΔT is temperature change; $\Delta \alpha = \alpha_s - \alpha_f$ is the difference in thermal expansion coefficients of the substrate ($\sim 13\text{--}16 \text{ }^\circ\text{C}^{-1}$ ppm) and the oxide scale ($\sim 8\text{--}9 \text{ }^\circ\text{C}^{-1}$ ppm). Temperature dependence of E_f and α is ignored. Accordingly, calculated average compressive stress values of σ_R are between -2.7 and -3.8 GPa. Experimentally measured values of residual stresses in the alpha alumina scale using XRD, optical fluorescence spectroscopy (OFS) and photo-simulated luminescence spectroscopy (PSLS) vary between -3 and -6 GPa depending on substrate and oxidation conditions [18,24,58,59]. If a representative value of $\sigma_R = -4$ GPa (assuming that internal stress remains constant) is summed with the compressive failure stress, the work of adhesion values presented in the Table 6 are obtained. These values show still the same trend for the specimens with a constant oxide thickness, but are appreciably higher. As a representative example, the values of W for specimen AM1-1 without σ_R are 2.2 J/m^2 (Eq. (6)) and 21.7 J/m^2 (Eq. (7)). With σ_R , the values increase to 39.1 and 90.3 J/m^2 respectively. Therefore, it is clearly shown that the evaluation of scale residual stress is crucial to calculate the work of adhesion.

It is obvious from Eqs. (6) and (7) that the W values are strongly affected by the magnitude of Young's modulus and the Poisson ratio. Young's modulus values for TGO alumina vary between 350 and 400 GPa, this can result in errors in W values calculated using Eqs. (6) and (7) of less than 10% and 8% respectively. However, if the film is represented by multi-layered oxides, the variations of

E_f and of Poisson ratio ν_f values, ν_f can lie between 0.2 and 0.28 according to the data reported in the literature for thermally grown $\alpha\text{-Al}_2\text{O}_3$ [39,60]. This uncertainty in the value of the Poisson ratio leads to errors of about $30\text{--}50\%$.

On the other hand, an error of about 10% may also arise from incorrect track width d measurement ($\pm 5 \text{ } \mu\text{m}$). Therefore, expected total error is $50\text{--}70\%$, which is still not as large as the effect of the internal residual stress in the oxide scale.

3.5.2. Effect of oxide scale thickness at constant S level

The work of adhesion W was calculated using Eqs. (6) and (7), for three different oxide scale thicknesses on AM1 (0.41 ppmw S). The two models show different tendencies (Table 4). The first model shows a slight increase of W with increasing the scale thickness when the second model leads to a large decrease of W from 11.4 J/m^2 (9 h) to 1.8 J/m^2 (330 h) with scale thickness, i.e. with the duration of oxidation. Model 2 is in agreement with the experimental observations showing that for a constant sulfur level and identical surface finish increasing of scale thickness causes the decrease of scale adhesion.

Values of the work of adhesion for AM1 (0.41 ppm S) estimated taking into account the residual stress $\sigma_R = -4$ GPa are reported in Table 6. The increase in thickness from 1.3 to $3.6 \text{ } \mu\text{m}$ results in an increase of the work of adhesion calculated using both equations (Table 6). This fact can be explained in terms of the predominant influence of the scale thickness on W values (over the failure stresses induced during the scratch test). As described in the previous section, more complex mechanical behavior was observed during the test in the case of MCNG samples. The values of the work of adhesion corresponding either to the entire oxide scale or only to the thickness of the internal alumina layer are summarized in Table 5. The work of adhesion, calculated using Model 1, increases with the total thickness and with the internal alumina layer thickness, but shows very small values. For example, for MCNG-3 with $0.2 \text{ } \mu\text{m}$ oxide thickness, a value $W = 0.1 \text{ J/m}^2$ was found. This is explained by the fact that W (Eq. (6)) is a strong function of the scratch track width. The larger the scratch track, the smaller the value for the work of adhesion W . Model 2 shows the same effect as in AM1, i.e. the adhesion degrades with the total oxide scale and with the thickness of the internal alumina layer. The value of W decreases until a critical thickness is exceeded. This fact has been confirmed by experimental observation. Whereas the value of the work of adhesion was found to be very small using Eq. (6) for MCNG-3 with a $0.2 \text{ } \mu\text{m}$ thick alumina layer, Eq. (7) gives a very high value for W . The explanation of such a result is the high ratio of critical force/ alumina layer cross-section area, which gives a high value of stress at failure.

3.5.3. Comparison of the two models and discussion on the validity of the results

The two models used to assess the adhesion work show the same tendency for sulfur content variation in accordance with cyc-

Table 6
Calculated values of the work of adhesion for AM1 samples, with or without considering the residual stresses.

AM1, sample No.	Model 1		Model 2			
	Failure stress, GPa	Work of adhesion W , J m^{-2}		Failure stress, GPa	Work of adhesion W , J m^{-2}	
		Without σ_R	With σ_R		Without σ_R	With σ_R
<i>Effect of sulfur content, $t = \text{const}$</i>						
1	1.2	2.2	39.1	3.9	21.7	90.3
3	1.1	2.0	44.5	2.6	11.4	74.5
7	1.8	1.8	42.8	1.9	6.5	59.5
<i>Effect of scale thickness, $S_{\text{content}} = \text{const}$</i>						
3	1.1	2.0	44.5	2.6	11.4	74.5
4	0.9	2.8	75.8	1.1	3.5	82.1
5	0.9	3.9	113.7	0.6	1.8	100.2

lic oxidation behaviors. Despite the fact that models lead to different values for the adhesion work, the scratch test, practiced under careful conditions on isothermally oxidized samples, can be used to predict qualitatively the long-term cyclic oxidation behavior of samples with varying chemical compositions. The adhesion behaviors regarding the effect of scale thickness was predicted differently using these models, especially for multilayered thermally grown oxides. From two models the Eq. (7) proposed by Attar and Johannesson [23] describes better the experimental observations showing the expected decrease of adhesion properties with the duration of oxidation.

It is important to point out that both models are based on elastically stored energy and use only the physical properties of the deposited film. The properties of the substrate are not incorporated into these models. The mechanism of delamination during the scratch test is much more complex and should certainly take into consideration the effect of substrate plastic deformation and stress state in the local contact zone between the indenter and the scratched surface. Models were developed to take the substrate into consideration, for example, Xie and Hawthorne proposed a scratch test analysis that estimated the strain field in the substrate [26] based on the contact mechanics of bulk materials as established by Herz and Bussinesk, a hemispherical model of elastic-plastic indentation referring to the work of Hill and Johnson [61,39]. The equation which was proposed includes the effects of the material properties of coating and substrate, of the indenter geometry and of the normal load, on the mean compressive coating stress. However, this equation is not suitable for comparing coatings of different thicknesses, or in different failure modes. Numerical simulations for the scratch test contact conditions have been made by developing a three-dimensional finite element model describing the elastic and plastic behaviors and calculating the stresses, strains, and fracture toughness for monolayer TiN-coating on steel [28].

The values of adhesion work obtained in the present study using the scratch test were compared to results obtained using the scratch test and other techniques for a thermally grown oxide scale on an alloy substrate. The order of magnitude of values obtained in the present study agrees with the investigation of [21,24,62–64] (Table 7). The authors related a relatively large distribution of values with mode mixity of fracture behavior and reported the fracture energy of alloy/alumina interfaces determined by a variety of methods to be between ~ 5 and 110 J/m^2 increasing from mode I to II accordingly.

The following conclusions can then be made from the previous analysis.

4. Conclusions

The growth kinetics of oxide scale during high-temperature isothermal oxidation of single-crystal superalloy AM1 with different sulfur concentrations (0.22–3.2 ppmw) and of MCNG were investigated at $1100 \text{ }^\circ\text{C}$. It was found that the oxidation kinetics of AM1 specimens were not monotonous functions of the sulfur level, and that there was no strong effect of S content on the isothermal oxide growth kinetics. The values of the parabolic constant k_p for the Hf-containing MCNG alloy are lower than those measured for all AM1 samples, in agreement with the well known effect of reactive elements on alpha alumina scale growth kinetics, but MCNG alloy shows faster transient oxidation than AM1. In addition, it was found that the surface finish (600 grit SiC or $1 \mu\text{m}$ diamond) had no effect on the oxidation kinetics.

The microstructures of the multi-layered oxide scales formed on both superalloys were characterized and compared. On AM1 alloy, the oxide consisted of an inner $\alpha\text{-Al}_2\text{O}_3$ layer and an outer NiAl₂O₄ spinel layer separated by a discontinuous rutile phase. Concerning MCNG alloy, the oxide scale is composed of three clearly distinguished layers: the inner adherent $\alpha\text{-Al}_2\text{O}_3$ layer, the upper NiO layer, and between them the double layered NiAl₂O₄ spinel separated by a discontinuous rutile layer with some Re- and Ru-rich oxide particles.

The ability of the scratch test technique to quantify the adherence of these complex oxide scales was evaluated. The existing models to quantify the interfacial adhesion of film/substrate systems were reviewed. In order to understand the problems which arise during the interpretation of scratch-test results, the two most commonly used models to assess the work of adhesion were chosen. Despite the fact that these models lead to different values for the adhesion work, they clearly show the same tendency for the effect of sulfur content. Sulfur decreases the critical load at failure of the oxide scale/substrate interface. The values of the work of adhesion were found to vary from 2.2 down to 1.8 J/m^2 (Eq. (6)) and from 21.7 down to 6.5 J/m^2 (Eq. (7)) with increasing sulfur level (0.22–3.2 ppmw). On the other hand, our analyses showed that there are many factors which can lead to large errors, especially in the case of multi-layered oxide scale, when the effect of the oxide scale thickness is analyzed. The sources of possible errors and imperfections of the models were discussed and the errors were quantified. An effect of oxidation duration on the adhesion behavior for this complex system was observed. Therefore a new model able to dissociate the effects of the time of oxidation and the effect of oxide scale thickness should be developed in future work.

Table 7
Values of energy release rate for different substrate/oxide scale systems.

Oxide/metal system	Value of energy release rate, J m^{-2}	Conditions of oxidation	Quantification methods/ mode of failure	Residual stress measurement method	Ref.
MA956 superalloy/alumina scale	28	Isothermal oxidation in lab. air at 1150 and $1250 \text{ }^\circ\text{C}$	Scratch test/wedge spallation	XRD	[24]
Substrate/alumina interface in TBC	$\sim 50\text{--}80$		Analytical treatment of the experimental data/wedge spallation	Model comprises the residual thermal strains	[62]
PWA 1484 (1.7 ppmS)/alumina scale	~ 93	Isothermal oxidation in lab. air at $1200 \text{ }^\circ\text{C}$	FEM calculations based on SEM observations/edge delamination	PSLS XRD	[21]
Fe–15Cr/chromia scale	20–80	Isothermal oxidation at 850 and $950 \text{ }^\circ\text{C}$ using a thermobalance under flowing Ar–15% O_2	Room temperature tensile testing in a SEM chamber	XRD, Raman spectroscopy	[64]
Pt-modified and Zr-doped $\beta\text{-NiAl}$ bond coat/alumina TGO	110–50	Cyclic oxidation $1100 \text{ }^\circ\text{C}$	Modified four-point bending test	PLPS	[63]

Using the isothermal oxidation kinetics and the oxide scale adhesion measurements, it can be concluded that the excellent cyclic oxidation behavior of bare MCNG alloy is partly due to lower long term oxidation kinetics but more importantly to the high adhesion of the thin alumina sublayer which is formed at its surface. It is confirmed that S strongly degrades the cyclic oxidation behavior of alloy AM1, i.e. an alloy without enough reactive element. This degradation is solely due to the decrease of the oxide scale adhesion, independently of its thickness. This is shown by scratch tests performed on samples with the same oxide scale thickness, and by thermogravimetry results showing that S does not increase the oxidation kinetics.

Acknowledgments

The authors gratefully acknowledge Diane Samelor (CIRIMAT laboratory) for her help in the scratch tests; Snecma-Safran Group (France) for providing samples of superalloys.

The work was partially supported by RUSERA.Exe. Project No. 043701 FP6 INCO, and the BQR-RI of INPT.

References

- [1] M.A. Smith, W.E. Frazier, B.A. Pregar, *Mater. Sci. Eng., A* 203 (1995) 388–398.
- [2] K. Bouhanek, D. Oquab, B. Pieraggi, *Mater. Sci. Forum* 251–254 (1997) 33–40.
- [3] J.G. Smeggil, A.W. Funkenbush, N.S. Bornstein, *Metall. Trans. A* 17 (1986) 923–932.
- [4] P.Y. Hou, J. Stringer, *Oxid. Met.* 38 (1992) 323–345.
- [5] S. Sarioglu, J.R. Blachere, F.S. Petit, G.H. Meier, J.L. Smialek, C. Mennicke, *Mater. Sci. Forum* 251–254 (1997) 405–412.
- [6] J.L. Smialek, B.A. Pint, *Mater. Sci. Forum* 369–372 (2001) 459–466.
- [7] B.A. Pint, I. Wright, W. Lee, Y. Zhang, K. Prubner, K. Alexander, *Mater. Sci. Eng. A245* (1998) 201–211.
- [8] P. Benjamin, C. Weaver, *Proc. R. Soc. A* 254 (1960) 163–176.
- [9] A.J. Perry, *Thin Solid Films* 107 (1983) 167–180.
- [10] M.T. Laugier, *Thin Solid Films* 117 (1984) 243–249.
- [11] J. Valli, U. Makela, M. Matthews, V. Murawa, *J. Vac. Sci. Technol., A* 3 (1985) 2411–2414.
- [12] P.A. Steinmann, Y. Tardy, H.E. Hintermann, *Thin Solid Films* 154 (1987) 403–416.
- [13] S.K. Venkataraman, D.L. Kohlstedt, W.W. Gerberich, *J. Mater. Sci.* 7 (1992) 1126–1132.
- [14] P.J. Burnett, D.S. Rickerby, *Thin Solid Films* 148 (1987) 41–50.
- [15] P.J. Burnett, D.S. Rickerby, *Thin Solid Films* 157 (1988) 233–254.
- [16] S.J. Bull, *Surf. Coat. Technol.* 50 (1991) 25–32.
- [17] J. Ast, D. Monceau, D. Oquab, CIRIMAT Toulouse, Unpublished Results, 2007.
- [18] D. Monceau, B. Pieraggi, *Oxid. Met.* 50 (1998) 477–493.
- [19] S. Hayashi, B. Gleeson, *Oxid. Met.* 71 (2009) 5–19.
- [20] J.A. Nychka, D.R. Clarke, G.H. Meier, *Mater. Sci. Eng., A* 490 (2008) 359–368.
- [21] C. Mennicke, M.-Y. He, D.R. Clarke, J.S. Smith, *Acta Mater.* 48 (2000) 2941–2949.
- [22] A.A. Volinsky, N.R. Moody, W.W. Gerberich, *Acta Mater.* 50 (2002) 441–466.
- [23] F. Attar, T. Johannesson, *Surf. Coat. Technol.* 78 (1996) 87–102.
- [24] S.J. Bull, *Tribol. Int.* 30 (1997) 491–498.
- [25] D.S. Rickerby, *Surf. Coat. Technol.* 36 (1998) 541–557.
- [26] Y. Xie, H.M. Hawthorne, *Surf. Coat. Technol.* 141 (2001) 15–25.
- [27] N.X. Randall, G. Favaro, C.H. Frankel, *Surf. Coat. Technol.* 137 (2001) 146–151.
- [28] K. Holmberg, A. Laukkanen, H. Ronkainen, K. Wallini, S. Varjus, *Wear* 254 (2003) 278–291.
- [29] J.-D. Kamminga, P. van Essen, R. Hoy, G.C.A.M. Janssen, *Tribol. Lett.* 19 (2005) 65–72.
- [30] H.S. Park, D. Kwon, *Thin Solid Films* 307 (1997) 156–162.
- [31] R.L. Browning, G.-T. Lim, A. Moyses, H.J. Sue, H. Chen, J.D. Earls, *Surf. Coat. Technol.* 201 (2006) 2970–2976.
- [32] M.D. Thouless, *Eng. Frac. Mech.* 61 (1998) 75–81.
- [33] S.J. Bull, E.J. Berasetegui, *Tribol. Int.* 39 (2006) 99–114.
- [34] A.A. Griffith, *Philos. Trans. R. Soc. London, Ser. A* 221 (1920) 163.
- [35] A.A. Griffith, *Proc. First Int. Congr. Appl. Mech. Delft* (1924) 55–63.
- [36] E. Orovan, *Weld. J.* 3 (1955) 157–160.
- [37] G.R. Irwin, in: *Proceedings of the ASM Symposium on Fracturing of Metals*, Cleveland, 1948, pp. 147–166.
- [38] G.M. Hamilton, L.E. Goodman, *J. Appt. Mech.* 33 (1966) 371–377.
- [39] K.L. Johnson, *Contact Mechanics*, Cambridge University Press, Cambridge, 1985.
- [40] K.A. Gruss, R.F. Davis, *Surf. Coat. Technol.* 114 (1999) 156–168.
- [41] S.S. Chiang, D.B. Marshall, A.G. Evans, *J. Appl. Phys.* 53 (1) (1982) 298–311.
- [42] J.W. Hutchinson, M.D. Thouless, E.G. Liniger, *Acta Metall. Mater.* 40 (1992) 295–308.
- [43] J.-S. Wang, A.G. Evans, *Acta Mater.* 46 (1998) 4993–5005.
- [44] H.E. Evans, *Intern. Mater. Rev.* 40 (1995) 1–40.
- [45] S.P. Timoshenko, *Theory of Elastic Stability*, McGraw-Hill, New York, 1936.
- [46] D.B. Marshall, A.G. Evans, *J. Appl. Phys.* 56 (10) (1984) 2632–2638.
- [47] L.G. Rosenfeld, J.E. Ritter, T.J. Lardner, M.R. Lin, *J. Appl. Phys.* 67 (7) (1990) 3291–3296.
- [48] S.J. Bull, D.S. Rickerby, A. Matthews, A. Leyland, A.R. Pace, J. Valli, *Surf. Coat. Technol.* 36 (1988) 503–517.
- [49] S.J. Bull, D.S. Rickerby, *Surf. Coat. Technol.* 42 (1990) 149–164.
- [50] P. Hadenqvist, M. Olsson, S. Jacobson, S. Soderberg, *Surf. Coat. Technol.* 41 (1990) 31–49.
- [51] J.F. Lin, C.C. Wei, Y.K. Yung, C.F. Ai, *Diamond Relat. Mater.* 13 (2004) 1895–1906.
- [52] S. Dreyepont, D. Monceau, F. Crabos, E. Andrieu, *Acta Mater.* 53 (2005) 4199–4209.
- [53] J.D. Kuenzly, D.L. Douglass, *Oxid. Met.* 8 (1974) 139–178.
- [54] P.Y. Hou, *J. Mater. Sci. Lett.* 19 (2000) 577.
- [55] R. Molins, A. Germidis, E. Andrieu, *Microscopy of Oxidation-3*, in: S.B. Newcomb, J.A. Little (Eds.), *Proc. Third International Conference on the Microscopy of Oxidation*, University of Cambridge, held during 16–18 September 1996, The Institute of Materials, London, 1997, p. 3.
- [56] R. Morrell, *Handbook of Properties of Technical and Engineering Ceramics*, HMSO, London, 1987.
- [57] K. Tien, J.M. Davidson, in: J.V. Cathcart (Ed.), *Stress Effects and the Oxidation of Metals*, AIME, 1975, pp. 200–219.
- [58] E. Schumann, C. Sarioglu, J.R. Blachere, F.S. Pettit, G.H. Meier, *Oxid. Met.* 53 (2000) 259–272.
- [59] D.M. Lipkin, D.R. Clarke, M. Hollatz, M. Bobeth, W. Pompe, *Corros. Sci.* 39 (1997) 231–242.
- [60] A.G. Evans, J.W. Hutchinson, M.Y. He, *Acta Mater.* 47 (5) (1999) 1513–1522.
- [61] R. Hill, *The Mathematical Theory of Plasticity*, Clarendon Press, Oxford, 1950.
- [62] M.R. Begley, D.R. Mumm, A.G. Evans, J.W. Hutchinson, *Acta Mater.* 48 (2000) 3211–3220.
- [63] P.-Y. Théry, M. Poulain, M. Dupeux, M. Braccini, *Surf. Coat. Technol.* 202 (2007) 648–652.
- [64] G. Bamba, Y. Wouters, A. Galerie, F. Charlot, A. Dellali, *Acta Mater.* 54 (2006) 3917–3922.